J. Fluid Mech. (2006), *vol.* 564, *pp.* 305–331. © 2006 Cambridge University Press
doi:10.1017/S0022112006001571 Printed in the United Kingdom

Internal wave fields generated by a translating body in a stratified fluid: an experimental comparison

By M. M. SCASE AND S. B. DALZIEL

Department of Applied Mathematics and Theoretical Physics, University of Cambridge, Centre for Mathematical Sciences, Wilberforce Road, Cambridge, CB3 0WA, UK

(Received 17 March 2005 and in revised form 15 March 2006)

Uniform approximations for the combined permanent and transient start-up waves produced by the impulsive motion of a body in a density-stratified fluid are calculated. These new approximations to the wave field remove the unphysically diverging fluid velocities and phase shifts near the boundary of the causality envelope associated with previous non-uniform approximations. The calculated wave field is compared to experimental measurements of the wave field generated by towing a spherical body through a linearly stratified fluid. Synthetic schlieren, a technique previously used only to analyse two-dimensional or axisymmetric flow, is developed further to allow comparison with this fully three-dimensional wave field. In particular, breadth averaging across the tank is employed. Good agreement is found between the theoretical and experimental results in the far field.

1. Introduction

Most studies of internal gravity waves generated by moving bodies within a stratified fluid concentrate on the so-called permanent waves built up by the sustained motion of the body. The flow is usually taken to be in a steady state and the transient start-up waves created by the initial movement of the body are ignored (e.g. Mowbray & Rarity 1967*a*, *b*; Lighthill 1978).

Transient and permanent waves were considered together for a horizontally towed body by Chashechkin & Makarov (1984), by use of a uniform expansion of the vertical displacement field. Sturova (1980) calculated the internal wave field for a disturbance accelerating linearly from rest, then moving at a constant speed before decelerating to rest. The problem of a body moving at steady velocity at arbitrary angle to the vertical was also considered in Sturova (1980) and an expression for the vertical displacement field was given.

A significant new approach to describing internal waves was taken by Voisin (1991, 1994) based on asymptotic approximations to internal potential fields described in terms of Green's functions. Voisin (1994) considered an arbitrarily moving point source and was able to write down a non-uniform approximation to the internal potential field with contributions both from the permanent waves, which are built up during the sustained motion of the source, and the transient 'start-up' waves, which are created as the source is impulsively started.

The present paper should be regarded as the second part of Scase & Dalziel (2004), in which a method was given for finding solutions for the permanent waves generated by a translating body, based on the general method of Voisin (1994). It was

https://doi.org/10.1017/S0022112006001571 Published online by Cambridge University Press

found, as in Sturova (1980), using the method of stationary phase, that at most three 'significant waves' contribute to the flow field at a given point in space. These waves were classified as upper flared, lower flared, upper cusped or lower cusped waves according to their position and shape. It was also shown that the permanent waves were contained within a region defined by causal restraints. This region was called the 'causality envelope'. A method was also described for easily modifying point-source approximations to the wave field to predict the wave field generated by a finite-sized source.

As a body is impulsively started, a fan of internal waves emanates from near its original position (e.g. Mowbray & Rarity 1967*a*; Bretherton 1967; Stevenson 1973; Lighthill 1978). These radiated waves have a broad frequency range. When experiments are conducted in a laboratory there are obvious physical restrictions on the maximum size of the tank that can be used. As such, for an impulsively started steadily translating body, a significant part of the field of view is situated outside the causality envelope, in a region where only the transient waves, due to the impulsive start-up, exist.

The present paper builds on previous analysis to show that for a useful approximation to the transient start-up waves, a uniform approximation, unlike that used by Voisin (1994), is required. It is shown that this new approximation preserves phase continuity across the boundary of the causality envelope (Scase 2003; Scase & Dalziel 2004). One problem with the Voisin's (1994) non-uniform approximation is that it predicts diverging velocities and a phase shift near the boundary of the causality envelope, meaning that any comparison with experimental data is not useful; this is avoided with the present exposition. It is also shown that the present uniform approximations, when applied, lead to a continuously differentiable wave field across the boundary of the causality envelope. The matching between the surfaces of constant phase for the permanent waves on one side and the transient waves on the other has been drawn theoretically and visualized experimentally in a number of two- and three-dimensional configurations by Stevenson (1973), Peat & Stevenson (1975) and Woodhead (1983). It was also drawn in figure 4 of Voisin (1994). In all cases, the phase discontinuity at the envelope was simply ignored.

Experiments are conducted using a development of the synthetic schlieren technique described in Dalziel, Hughes & Sutherland (2000). All existing synthetic schlieren methods are either two-dimensional (e.g. Sutherland *et al.* 1999; Dalziel *et al.* 2000; Sutherland *et al.* 2000) or are restricted to axisymmetric three-dimensional configurations (Flynn, Onu & Sutherland 2003). By considering the three-dimensional flow in the experimental tank to be made up of many thin two-dimensional flows arranged next to each other, the equations which govern synthetic schlieren calculations are solved. This approach allows breadth-averaged measurements to be made of completely general three-dimensional flows. A comparison is made between the velocity fields predicted by the theory and the experimental values and the agreement is shown to be good.

It will be assumed throughout that the fluid is inviscid, incompressible, unbounded and has a uniform stratification $\rho_0(z) = \rho_{00} \exp\{-\beta z\}$, where $\beta g = N^2$. Here, N is the constant buoyancy frequency defined by

$$N^2 = -\frac{g}{\rho_0}\frac{\mathrm{d}\rho_0}{\mathrm{d}z},$$

g is the acceleration due to gravity, ρ_{00} is a reference density and $\rho_0(z)$ is the background, hydrostatic density field. The 'well-known' Boussinesq approximation

https://doi.org/10.1017/S0022112006001571 Published online by Cambridge University Press

(Boussinesq 1903) is made whereby density differences in the inertial and viscous terms of the Navier–Stokes momentum equation are ignored.

The relevant non-dimensional parameters characterizing the flows considered are the Reynolds and Froude numbers defined respectively as

$$\mathscr{R} = \frac{2v_0 a}{\nu}, \qquad \mathscr{F} = \frac{v_0}{Na}, \tag{1.1}$$

where a is the characteristic length scale of the body being towed, e.g sphere radius. Non-dimensionalization is as follows:

$$\boldsymbol{r}_\star = \frac{N\boldsymbol{r}}{v_0}, \qquad \boldsymbol{u}_\star = \frac{\boldsymbol{u}}{v_0}, \qquad t_\star = tN, \tag{1.2}$$

where $v_0 = |\boldsymbol{v}_0|$.

In § 2 the theoretical background established in Voisin (1994) and Scase & Dalziel (2004) is briefly recapped and the key results from these papers are given. In § 2.2 a composite uniform approximation for the wave field is derived; this is compared to the more general uniform expansion in § 2.3 and § 2.4. In § 2.5 the modification from the point-source solutions to finite-sized body solutions is discussed as is wave attenuation due to viscous effects. In § 3 the experimental technique is discussed. A brief overview of two-dimensional synthetic schlieren is provided in § 3.1 and this is extended in § 3.2 for use with fully three-dimensional flows. Results are presented in § 4 and conclusions are stated in § 5.

2. Theoretical background

In Scase & Dalziel (2004) a method was given for finding solutions for the permanent waves generated by a translating body in a stratified fluid based on the general method of Voisin (1994). The notation and geometrical set-up in the present paper is the same as in both previous papers. The essential details are repeated here for clarity.

2.1. *Geometrical set-up*

The velocity, $\boldsymbol{u}(\boldsymbol{r}, t)$, and pressure perturbation, $p'(\boldsymbol{r}, t)$, fields can be written in terms of a scalar 'internal potential', $\Psi(\boldsymbol{r}, t)$, as (Gorodtsov & Teodorovich 1980; Hart 1981)

$$\boldsymbol{u}(\boldsymbol{r}, t) = \left(\frac{\partial^2}{\partial t^2}\nabla + N^2\nabla_h\right)\psi(\boldsymbol{r}, t), \qquad p'(\boldsymbol{r}, t) = -\rho_0\left(\frac{\partial^2}{\partial t^2} + N^2\right)\frac{\partial}{\partial t}\psi(\boldsymbol{r}, t), \tag{2.1}$$

where $\nabla_h = (\partial_x, \partial_y, 0)$. Such a representation is possible because the wave motion has zero linearized potential vorticity $(\nabla \times \boldsymbol{u})\cdot\nabla\rho/\rho_{00}$ (M. E. McIntyre, personal communication), which follows from the linearized Euler equations. Taking the curl of the velocity in (2.1) shows

$$\boldsymbol{\omega}(\boldsymbol{r}, t) = N^2\left(-\frac{\partial}{\partial y}, \frac{\partial}{\partial x}, 0\right)\frac{\partial}{\partial z}\psi(\boldsymbol{r}, t), \tag{2.2}$$

which is approximately perpendicular to the gradient of the density field, $\nabla\rho$, since the horizontal gradients of the density field are small. Hence the use of a potential function of the form given in (2.1) is possible. The perturbation to the background density field is given by

$$\rho'(\boldsymbol{r}, t) = \frac{N^2\rho_0}{g}\frac{\partial^2}{\partial t\,\partial z}\psi(\boldsymbol{r}, t). \tag{2.3}$$

https://doi.org/10.1017/S0022112006001571 Published online by Cambridge University Press

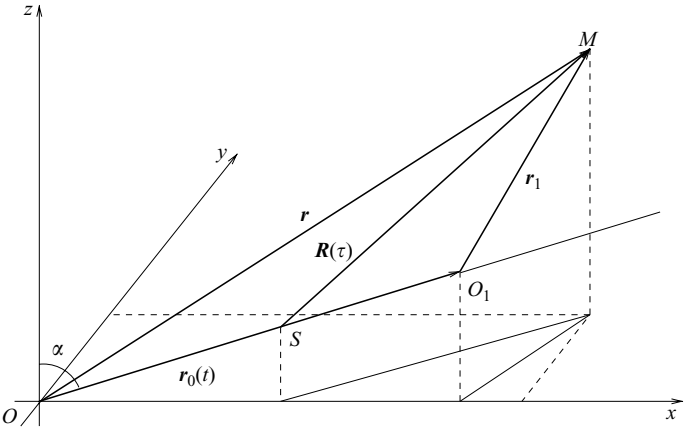


FIGURE 1. The geometrical set-up.

The internal potential satisfies the continuity equation

$$\nabla \cdot \boldsymbol{u} \equiv \left(\frac{\partial^2}{\partial t^2} \nabla^2 + N^2 \nabla_h^2 \right) \psi(\boldsymbol{r}, t) = m(\boldsymbol{r}, t), \tag{2.4}$$

where m is the mass source term.

The moving point source, at position $\boldsymbol{r}_0(t)$, say, has the form

$$m(\boldsymbol{r}, t) = m_0(t) \delta(\boldsymbol{r} - \boldsymbol{r}_0(t)) H(t), \tag{2.5}$$

where δ is the Dirac delta function and H is the Heaviside step function. The main interest will be in the case of a source translating steadily, with constant velocity $\boldsymbol{v}_0$, so that $\mathrm{d}\boldsymbol{r}_0(t)/\mathrm{d}t = \boldsymbol{v}_0$ for $t > 0$. Point-source models have been successfully used by previous authors to model flows generated by bodies of finite extent (e.g. Mowbray & Rarity 1967*a*, *b*; Stevenson 1968; Lighthill 1978).

The coordinates used are shown in figure 1. The origin O is fixed. At time t the mass source is at O_1 having position vector $\boldsymbol{r}_0(t)$. Voisin's (1994) calculation considers the waves emitted at time τ, from the point S, say, lying between O and O_1, and reaching M at time $t > \tau$, where M has position vector $\boldsymbol{r} = \boldsymbol{r}_0(\tau) + \boldsymbol{R}(\tau) = \boldsymbol{r}_0(t) + \boldsymbol{r}_1$, in the notation of the figure. It will be useful to regard $\boldsymbol{r}_1$ as position in a moving set of coordinates with origin O_1.

The asymptotic expression for the internal potential is the result of summing all the contributions from the source between $\tau = 0$ and $\tau = t$, namely (Voisin 1994)

$$\psi(\boldsymbol{r}, t) \sim -\frac{1}{(2\pi)^{3/2} N} \int_0^t \frac{m_0}{R_h(\tau)} \left\{ \frac{\cos\left[(t-\tau) N \dfrac{|R_z(\tau)|}{R(\tau)} - \dfrac{\pi}{4} \right]}{\left[(t-\tau) N \dfrac{|R_z(\tau)|}{R(\tau)} \right]^{1/2}} + \frac{\sin\left[(t-\tau) N - \dfrac{\pi}{4} \right]}{[(t-\tau)N]^{1/2}} \right\} \mathrm{d}\tau, \tag{2.6}$$

valid for $(t - \tau)N \gg 1$, where $\boldsymbol{R}(\tau) = (R_x, R_y, R_z)$, $\boldsymbol{R}_h(\tau) = (R_x, R_y, 0)$, $R(\tau) = |\boldsymbol{R}(\tau)|$ and $R_h(\tau) = |\boldsymbol{R}_h(\tau)|$. The cosine term represents internal gravity waves of frequency $\omega = R_z(\tau) N / R(\tau)$ propagating at an angle φ to the vertical where $\cos\varphi = R_z(\tau)/R(\tau)$.

https://doi.org/10.1017/S0022112006001571 Published online by Cambridge University Press

Contributions to this integral are separated naturally into those from buoyancy oscillations with frequency N and gravity waves. The gravity waves have a phase, Φ, given by

$$\Phi = \frac{(t-\tau)N|R_z(\tau)|}{R(\tau)}. \tag{2.7}$$

Voisin (1994) makes asymptotic approximations to the internal potential integral (2.6) in order to describe the flow field. In particular, the stationary phase contributions describe the so-called permanent wave field made up of those waves 'continuously built up by the motion of the source'. The asymptotic approximation to the internal potential field for the permanent waves is a Liénard–Wiechert potential (Reitz & Milford 1960). The expression for the permanent waves is given in terms of a retarded time, $\tau = \tau_s$. This retarded time is the time at which the wave which reaches M at time t was emitted from S. The retarded time is found from the stationary phase condition $\partial\Phi/\partial\tau|_{\tau=\tau_s} = 0$ and is given by solutions of

$$t - \tau_s = \frac{R(\tau_s)}{\boldsymbol{v}_0(\tau_s)\cdot\left[\dfrac{\boldsymbol{R}(\tau_s)}{R(\tau_s)} - \dfrac{R(\tau_s)}{R_z(\tau_s)}\hat{\boldsymbol{e}}_z\right]}. \tag{2.8}$$

The expression for the internal potential for the permanent waves is then given by (Voisin 1994)

$$\psi_p(\boldsymbol{r}, t) \sim -\frac{m_0(\tau_s)}{2\pi N^2|A|^{1/2}}\frac{R(\tau_s)}{R_h(\tau_s)|R_z(\tau_s)|}\cos\left[\frac{N}{c_g}|R_z(\tau_s)| - \frac{\pi}{2}H(-A)\right], \tag{2.9}$$

where $c_g = |\boldsymbol{c}_g|$ is the modulus of the group velocity given by

$$\boldsymbol{c}_g(\tau_s) = \frac{\boldsymbol{R}(\tau_s)}{t-\tau_s} = \boldsymbol{v}_0(\tau_s)\cdot\left[\frac{\boldsymbol{R}(\tau_s)}{R(\tau_s)} - \frac{R(\tau_s)}{R_z(\tau_s)}\hat{\boldsymbol{e}}_z\right]\frac{\boldsymbol{R}(\tau_s)}{R(\tau_s)}, \tag{2.10}$$

the unit vertical vector is denoted by $\hat{\boldsymbol{e}}_z$ and

$$A = R\frac{\boldsymbol{\gamma_0}}{c_g^2}\cdot\left(\frac{\boldsymbol{R}}{R} - \frac{R}{R_z}\hat{\boldsymbol{e}}_z\right) - \left(\frac{\boldsymbol{v}_0}{c_g}\times\frac{\boldsymbol{R}}{R}\right)^2 + 2\frac{\boldsymbol{v}_0}{c_g}\cdot\frac{R}{R_z}\hat{\boldsymbol{e}}_z\Big|_{\tau=\tau_s}. \tag{2.11}$$

Here $\boldsymbol{\gamma}_0(t) = \mathrm{d}^2\boldsymbol{r}_0/\mathrm{d}t^2$ is the acceleration of the source. The quantity A is derived from the second derivative of the phase, Φ, specifically

$$\frac{\partial^2\Phi}{\partial\tau^2}\Big|_{\tau=\tau_s} = \frac{N|R_z(\tau_s)|c_g(\tau_s)}{R(\tau_s)^2}A. \tag{2.12}$$

Furthermore, (2.3) implies that for permanent waves

$$\rho_p'(\boldsymbol{r}, t) \sim \frac{m_0(\tau_s)N^2\rho_0}{2\pi g}\frac{R_h(\tau_s)|R_z(\tau_s)|}{R(\tau_s)^2R_z(\tau_s)}\frac{1}{c_g|A|^{1/2}}\cos\left[\frac{N}{c_g}|R_z(\tau_s)| - \frac{\pi}{2}H(-A)\right]. \tag{2.13}$$

Voisin's (1994) non-uniform approximation for the internal potential, ψ, is split into two parts: a permanent wave contribution (2.9) and a transient wave contribution. An expression for the internal potential for these transient waves, $\psi_t(\boldsymbol{r}, t)$, is given in

https://doi.org/10.1017/S0022112006001571 Published online by Cambridge University Press

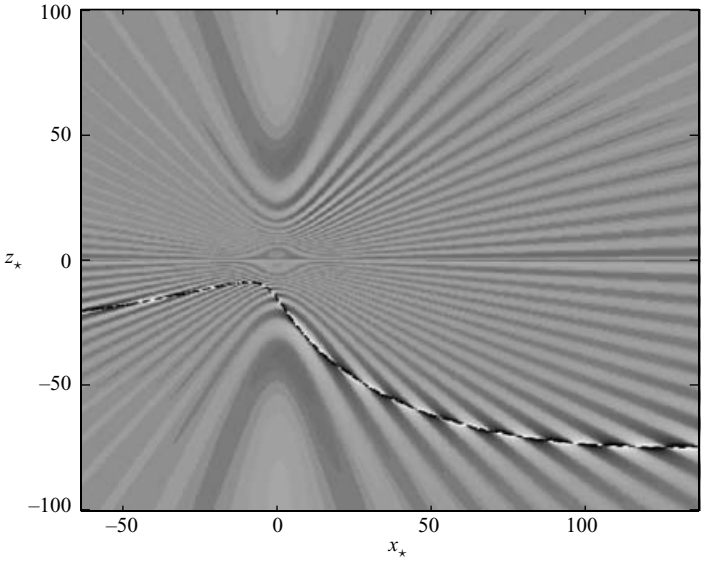


FIGURE 2. Voisin's (1994) model of transient start-up waves, showing the diverging internal potential near the boundary of the causality envelope (dashed black line). This leads to unphysically large velocities predicted in the flow field. In the figure, a point source of strength 1 was started with tow angle $\alpha = \pi/3$. The plane shown is $y_\star = 10$ at $t_\star = 100$. The colour scale is shown in figure 3.

equation (3.9) of Voisin (1994), namely

$$\psi(\boldsymbol{r}, t) \sim -\frac{m_0(0)}{(2\pi)^{3/2} N^2 r_h} \frac{\dfrac{r}{|z|}}{1 - \dfrac{\boldsymbol{v}_0(0)t}{r} \cdot \left(\dfrac{\boldsymbol{r}}{r} - \dfrac{r}{z}\hat{\boldsymbol{e}}_z\right)} \frac{\sin\left(\dfrac{Nt|z|}{r} - \dfrac{\pi}{4}\right)}{\left(\dfrac{Nt|z|}{r}\right)^{1/2}} + \frac{m_0(0)}{(2\pi)^{3/2} N^2 r_h} \frac{\cos\left(Nt - \dfrac{\pi}{4}\right)}{(Nt)^{1/2}}, \quad (2.14)$$

where $r = |(x, y, z)|$ is the distance from M to the origin O in figure 1, $r_h = |(x, y, 0)|$ and $\hat{\boldsymbol{e}}_z$ is a unit vector in the vertical. The internal potential due to (2.14) is shown in figure 2. The body was started at time $t_\star = 0$ at position $\boldsymbol{r}_\star = \boldsymbol{0}$ and is now, at time $t_\star = 100$, at $\boldsymbol{r}_\star \approx (87, 0, 50)$. Only the internal potential field in the plane $y_\star = 10$ is shown. The dashed curve shows the position of the causality envelope. Near to this curve the magnitude of the internal potential diverges.

This expression relies on a linear approximation of the phase of the gravity waves as

$$\Phi(\tau) = \lambda g(\tau) \sim \lambda(g(0) + \tau g'(0)), \quad (2.15)$$

where $\lambda = Nt$, a prime indicates differentiation with respect to τ and

$$g(\tau) = \left(1 - \frac{\tau}{t}\right) \frac{|R_z(\tau)|}{R(\tau)}. \quad (2.16)$$

Permanent waves of a given frequency, and therefore a given angle of propagation, are contained within a region bounded by the origin of the moving set of coordinates O_1

https://doi.org/10.1017/S0022112006001571 Published online by Cambridge University Press



FIGURE 3. Grey scaling for figures 2, 4, 6 and 7, where ψ has been normalized by $m_0/(Nv_0)$.

and the 'causality envelope'. The causality envelope is so called because the boundary is defined by the distance the permanent waves which were created at $t=0$ have travelled, so it is the boundary between permanent waves 'created' for $t<0$ and for $t>0$.

Equation (2.14) is equivalent to

$$\psi_t(\boldsymbol{r},t) \sim \frac{m_0(0)}{(2\pi)^{3/2}Nr_h}\frac{1}{(\lambda g(0))^{1/2}(\lambda g'(0))}\sin\left(\lambda g(0)-\frac{\pi}{4}\right)+\frac{m_0(0)}{(2\pi)^{3/2}N^2r_h}\frac{\cos\left(\lambda-\dfrac{\pi}{4}\right)}{\lambda^{1/2}}. \tag{2.17}$$

However, it is immediately clear that this expression is not defined on the surface $\lambda g'(0)=0$ and this is exactly the boundary of the 'causality envelope' given by the real roots of

$$[z+v_{0z}(0)t]x^2-[v_{0x}(0)tz]x+[z^3+y^2\{z+v_{0z}(0)t\}]=0. \tag{2.18}$$

Equation (2.18) can be derived directly from setting $g'(0)=0$ or from the expression given on p. 301 of Scase & Dalziel (2004). In the special case of horizontal towing, (2.18) reduces to

$$\left(x-\frac{v_{0x}(0)t}{2}\right)^2+y^2+z^2=\left(\frac{v_{0x}(0)t}{2}\right)^2 \tag{2.19}$$

showing that in this case the causality envelope is a sphere with diameter $v_{0x}(0)t$ which intersects with O and O_1, as was shown in Voisin (1994).

Hope for obtaining a comparison of the combined permanent waves and transient waves with any experimental evidence near the causality envelope, using (2.14), is therefore lost. Figure 2 shows the divergence of the internal potential field near the boundary of the causality envelope (dashed black line) for a steadily towed body.

It should be noted that the expression for the permanent wave field (2.9) is a non-uniform approximation. Evaluation of (2.9) requires solving (2.8) which can be written as a cubic polynomial (equation (3.7) in Scase & Dalziel 2004). This cubic has either one real root or three real roots and a caustic exists in the approximated flow field where the number of real roots of the cubic changes. Equivalently, as two real roots of (2.8) coalesce, the quantity A in (2.9) tends to 0. This leads to another unphysical singularity in the approximated flow field. However, this singularity is confined to a much smaller surface than the singularity at the causality envelope. Removal of the caustic singularity would require a uniform expansion in terms of Airy functions and has not been attempted here. These singularities are not visible in the experimental comparison (figures 9, 11) since the singularity occurs very abruptly near the caustic and unless the field is evaluated at exactly the caustic, the process of breadth averaging (see § 3) removes any notable singularities. This is not true of the non-uniform approximation to the transient wave field where a very clear singularity in the wave field is observed around the causality envelope even after a breadth averaging process.

https://doi.org/10.1017/S0022112006001571 Published online by Cambridge University Press

2.2. *Composite uniform approximation to the wave field*

In order to remove the unphysically large velocities (figure 2) associated with the non-uniform approximation to the wave field, uniformly valid approximations to the wave field are sought. In this section this goal is achieved by deriving a uniformly valid composite approximation to the wave field, separating the permanent waves from those due to the initial transient. As is shown later (§ 2.4) there are some advantages to this formulation when compared with an approximation derived (in § 2.3) from a general uniform expansion of the equations.

We consider the gravity wave contribution to the internal potential given by $\psi_{gw} = \mathrm{Re}\,\Psi_{gw}$, where

$$\Psi_{gw} \sim \int_0^t f(\tau)\exp\left\{\mathrm{i}\left[\lambda g(\tau) - \frac{\pi}{4}\right]\right\}\mathrm{d}\tau, \tag{2.20}$$

and the amplitude and the phase are defined respectively as

$$f(\tau) = -\frac{m_0(\tau)}{(2\pi)^{3/2} N R_h(\tau)[\lambda g(\tau)]^{1/2}}, \quad g(\tau) = \left(1 - \frac{\tau}{t}\right)\frac{|R_z(\tau)|}{R(\tau)}. \tag{2.21}$$

It follows that

$$f(0) = -\frac{m_0(0) r^{1/2}}{(2\pi)^{3/2} N r_h [\lambda|z|]^{1/2}}, \tag{2.22}$$

$$g(0) = \frac{|z|}{r}, \tag{2.23}$$

$$g'(0) = \frac{|z|}{rt}\left[\frac{\boldsymbol{v}_0(0)t}{r}\cdot\left(\frac{\boldsymbol{r}}{r} - \frac{r}{z}\hat{\boldsymbol{e}}_z\right) - 1\right], \tag{2.24}$$

$$g''(0) = \frac{|z|}{rt^2}\left[3\left(\frac{\boldsymbol{r}\cdot\boldsymbol{v}_0(0)t}{r^2}\right)^2 - \left(\frac{\boldsymbol{v}_0(0)t}{r}\right)^2 + 2\frac{\boldsymbol{v}_0(0)t\cdot\hat{\boldsymbol{e}}_z}{z} - 2\left(\frac{r}{z}\boldsymbol{v}_0(0)t\cdot\hat{\boldsymbol{e}}_z + r\right)\frac{\boldsymbol{r}\cdot\boldsymbol{v}_0(0)t}{r^3} + \frac{\boldsymbol{\gamma}_0(0)t^2}{r}\cdot\left(\frac{\boldsymbol{r}}{r} - \frac{r}{z}\hat{\boldsymbol{e}}_z\right)\right] \tag{2.25}$$

The non-uniform expressions for the internal potential derived in Voisin (1994) are, in the present notation, for $\tau_s \neq 0$,

$$\Psi_{gw} \sim \sqrt{\frac{2\pi}{\lambda|g''(\tau_s)|}} f(\tau_s)\exp\left\{\mathrm{i}\left[\lambda g(\tau_s) - \frac{\pi}{2}H(-g''(\tau_s))\right]\right\}H(\tau_s) + \mathrm{i}\frac{f(0)}{\lambda g'(0)}\exp\left\{\mathrm{i}\left[\lambda g(0) - \frac{\pi}{4}\right]\right\} \tag{2.26a}$$

where the first term is referred to as the permanent wave contribution and the second term is referred to as the transient wave contribution. If $\tau_s = 0$ then

$$\Psi_{gw} \sim \sqrt{\frac{\pi}{2\lambda|g''(0)|}} f(0)\exp\left\{\mathrm{i}\left[\lambda g(0) - \frac{\pi}{2}H(-g''(0))\right]\right\}. \tag{2.26b}$$

However, these expressions (2.26) are not uniformly valid as $\tau_s \to 0$, i.e. as we approach the causality envelope in space for a given time.

A locally uniform approximation in the neighbourhood of the causality envelope can be found by adapting Lighthill's (1978, § 4.11) approach for dealing with caustics. If the stationary phase point, τ_s, approaches the endpoint $\tau = 0$, the phase can be

https://doi.org/10.1017/S0022112006001571 Published online by Cambridge University Press

approximated by the quadratic expression

$$g(\tau) \sim g(0) + \tau g'(0) + \frac{\tau^2}{2} g''(0). \tag{2.27}$$

Hence we have approximately,

$$\begin{aligned}\Psi_{gw} &\sim f(0) \int_0^\infty \exp\left\{ \mathrm{i} \left[\lambda \left(g(0) + g'(0)\tau + g''(0)\frac{\tau^2}{2} \right) - \frac{\pi}{4} \right] \right\} \mathrm{d}\tau \\ &= \sqrt{\frac{\pi}{2\lambda |g''(0)|}} f(0) \exp\left\{ \mathrm{i} \left[\lambda \left(g(0) - \frac{g'(0)^2}{2g''(0)} \right) - \frac{\pi}{2} H(-g''(0)) \right] \right\} \\ &\quad \times \left\{ 1 - [1 - \mathrm{i}\,\mathrm{sgn}(g''(0))][\mathscr{C} + \mathrm{i}\,\mathrm{sgn}(g''(0))\mathscr{S}] \left(\sqrt{\frac{\lambda g'(0)^2}{\pi |g''(0)|}} \right) \mathrm{sgn}(g'(0)g''(0)) \right\},\end{aligned} \tag{2.28}$$

where

$$\mathscr{C}(\tau) = \int_0^\tau \cos\left(\frac{\pi x^2}{2} \right) \mathrm{d}x, \quad \mathscr{S}(\tau) = \int_0^\tau \sin\left(\frac{\pi x^2}{2} \right) \mathrm{d}x, \tag{2.29}$$

are the well-known Fresnel integrals. It can be shown that the limit of (2.28) for $\tau_s \neq 0$ as $\lambda \to \infty$ is given by

$$\begin{aligned}\Psi_{gw} \sim f(0) \sqrt{\frac{2\pi}{\lambda\, |g''(0)|}} \exp\left\{ \mathrm{i} \left[\lambda g(0) - \frac{g'(0)^2}{2g''(0)} \right] - \frac{\pi}{2} H(-g''(0)) \right\} H[-g'(0)g''(0)] \\ + \mathrm{i} \frac{f(0)}{\lambda g'(0)} \exp\left\{ \mathrm{i} \left[\lambda g(0) - \frac{\pi}{4} \right] \right\},\end{aligned} \tag{2.30}$$

a superposition of $O(\lambda^{-1/2})$ permanent waves and $O(\lambda^{-1})$ transient waves. If $\tau_s = 0$ in (2.28) then $g'(0) = 0$ and we recover (2.26*b*).

Note that if $\tau_s \sim 0$, then the expansion of the phase (2.27) shows that

$$\tau_s \sim -\frac{g'(0)}{g''(0)}, \quad g(\tau_s) \sim g(0) - \frac{g'(0)^2}{2g''(0)}. \tag{2.31}$$

It follows from substitution of (2.31) into (2.26*a*) that the common form of both the non-uniform approximation (2.26*a*) and the locally uniform approximation (2.28) in the vicinity of the causality envelope as $\lambda \to \infty$ is given by (2.30).

We now construct a uniformly valid composite solution for the wavefield based on the non-uniform approximation in (2.26*a*), the 'outer solution' and the locally uniform approximations (2.28), the 'inner solution'. This composite uniform approximation is made by adding the inner and outer solutions together and subtracting their common form (2.30) in the overlapping region, close to the causality envelope (see e.g. Hinch 1991). This yields the uniformly valid composite approximation to the gravity wave internal potential, given by

$$\begin{aligned}\Psi_{gw} &\sim \sqrt{\frac{2\pi}{\lambda |g''(\tau_s)|}} f(\tau_s) \exp\left\{ \mathrm{i} \left[\lambda g(\tau_s) - \frac{\pi}{2} H(-g''(\tau_s)) \right] \right\} H(\tau_s) \\ &\quad + \sqrt{\frac{\pi}{2\lambda |g''(0)|}} f(0) \exp\left\{ \mathrm{i} \left[\lambda \left(g(0) - \frac{g'(0)^2}{2g''(0)} \right) - \frac{\pi}{2} H(-g''(0)) \right] \right\} \mathrm{sgn}(g'(0)g''(0)) \\ &\quad \times \left\{ 1 - [1 - \mathrm{i}\,\mathrm{sgn}(g''(0))][\mathscr{C} + \mathrm{i}\,\mathrm{sgn}(g''(0))\mathscr{S}] \left(\sqrt{\frac{\lambda g'(0)^2}{\pi |g''(0)|}} \right) \right\}.\end{aligned} \tag{2.32}$$

https://doi.org/10.1017/S0022112006001571 Published online by Cambridge University Press

If both sgn(0) and $H(0)$ are defined such that $\mathrm{sgn}(0)=0$ and $H(0)=1/2$, then (2.32) is uniformly valid for all τ_s.

The approximation (2.32) has several appealing properties. The first term is simply the permanent wave contribution of the non-uniform approximation (2.9) and (2.26*a*) calculated by Voisin (1994). Hence, in regions where more than one permanent wave contributes to the wave field (cf. 'regions of interference' Scase & Dalziel 2004), the additional waves may simply be superposed onto the wave field as before. The second term may be loosely regarded as 'the transient wave field', equivalent to the $O(\lambda^{-1})$ term in (2.26*a*), and will be referred to as such hereafter for simplicity. However, this second term, whilst certainly containing the transient wave field, is of $O(\lambda^{-1/2})$ and can significantly contribute to the permanent wave field. As such this second term does not strictly contain only transient waves. Instead of diverging and having a phase shift at the causality envelope as the non-uniform approximation does, the composite uniform approximation is both continuous and differentiable.

The complete wave field, including permanent waves, the newly derived approximation for transient gravity waves and transient buoyancy oscillations is given by $\psi=\mathrm{Re}\,\Psi$, where

$$\begin{aligned}\Psi(\boldsymbol{r},t)\sim{}&\sqrt{\frac{2\pi}{\lambda|g''(\tau_s)|}}f(\tau_s)\exp\left\{\mathrm{i}\left[\lambda g(\tau_s)-\frac{\pi}{2}H(-g''(\tau_s))\right]\right\}H(\tau_s)\\&+\sqrt{\frac{\pi}{2\lambda|g''(0)|}}f(0)\exp\left\{\mathrm{i}\left[\lambda\left(g(0)-\frac{g'(0)^2}{2g''(0)}\right)-\frac{\pi}{2}H(-g''(0))\right]\right\}\\&\times\mathrm{sgn}(g'(0)g''(0))\left\{1-[1-\mathrm{i}\,\mathrm{sgn}(g''(0))][\mathscr{C}+\mathrm{i}\,\mathrm{sgn}(g''(0))\mathscr{S}]\left(\sqrt{\frac{\lambda g'(0)^2}{\pi|g''(0)|}}\right)\right\}\\&+\frac{m_0(0)}{(2\pi)^{3/2}N^2r_h}\frac{\cos\left(\lambda-\dfrac{\pi}{4}\right)}{\lambda^{1/2}}.\end{aligned}\tag{2.33}$$

The wave field may be constructed exactly as before, with the permanent wave contributions being included only when $0\leqslant\tau_s\leqslant t$, and two additional terms representing the transient wave field generated by the impulsive start-up motion.

Making the comparison between the new transient wave approximation (the second and third terms in (2.33)) (figure 4) with Voisin's previous model (2.14) (figure 2) shows why the uniform approximation is required if comparison is to be made with experiment. With the non-uniform approximation a banding appears near the boundary of the causality envelope where the internal potential for the transient waves diverges. This is shown more clearly in figure 5. The internal potential field has been plotted for $x_\star\approx 36$, $y_\star=10$, $t_\star=100$ for both non-uniform (dashed) and composite uniform (solid) approximations. Away from the causality envelope both approximations coincide as expected. However, close to the causality envelope ($z_\star\approx -55$) the non-uniform approximation diverges.

Figure 6 shows the internal potential in the $y_\star=10$ plane for the permanent wave field, calculated using the method described in Scase & Dalziel (2004). In figure 7 the permanent waves are now added to the new transient wave terms in (2.33) showing the full composite uniform approximation to the internal potential function (2.6). With the composite uniform approximation to the transient wave field, the amplitude of the combined wave field remains continuous and differentiable across the boundary, and the phases match.

https://doi.org/10.1017/S0022112006001571 Published online by Cambridge University Press

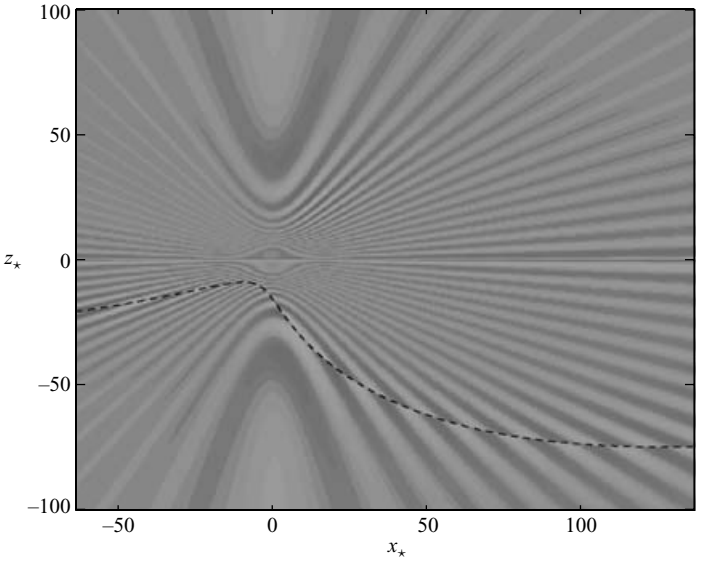


FIGURE 4. The composite uniform internal potential field for transient start-up waves. The field show has the same initial parameters as in figure 2. With the composite approximation, divergence of the internal potential only occurs near $g'(0)g''(0) = 0$.

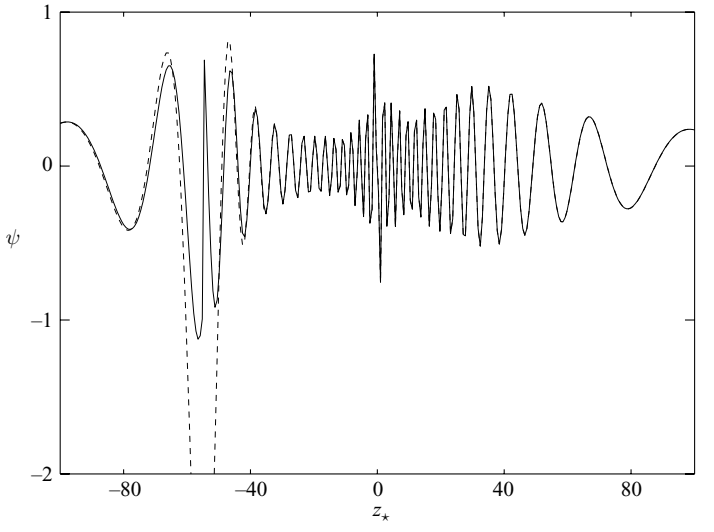


FIGURE 5. The divergence of the non-uniform approximation is clearly shown by plotting the internal potentials from figure 4 (solid) and figure 2 (dashed). Away from the causality envelope near $z_\star \approx -55$ the two solutions coincide, but near the causality envelope the non-uniform solution diverges.

2.3. *General uniform expansion*

An alternative approach to those discussed in § 2.2 is to use a general uniform expansion of (2.6) that treats both sets of permanent and transient waves together. This is equivalent to approximating (2.6) by considering the endpoint contribution from $\tau = 0$ and the stationary phase contribution from $\tau = \tau_s$ together. A suitable

https://doi.org/10.1017/S0022112006001571 Published online by Cambridge University Press

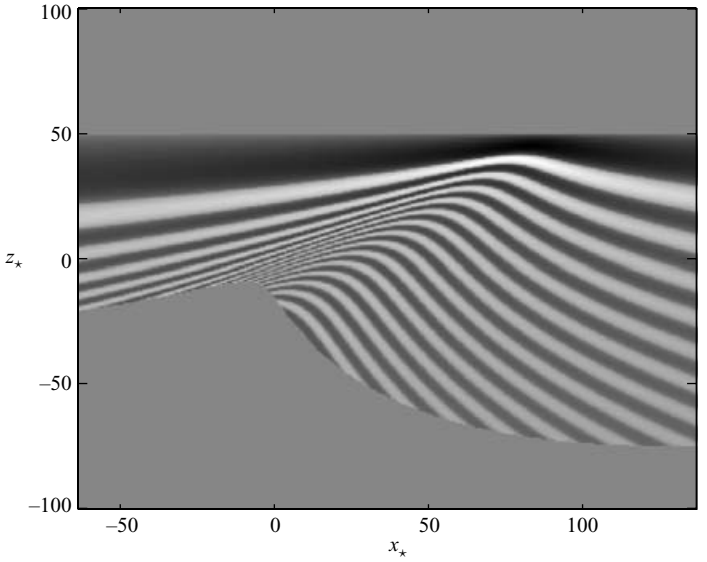


FIGURE 6. The internal potential field for the permanent waves. The point source was towed with $\alpha = \pi/3$. The field shown is at $t_\star = 100$ and $y_\star = 10$.

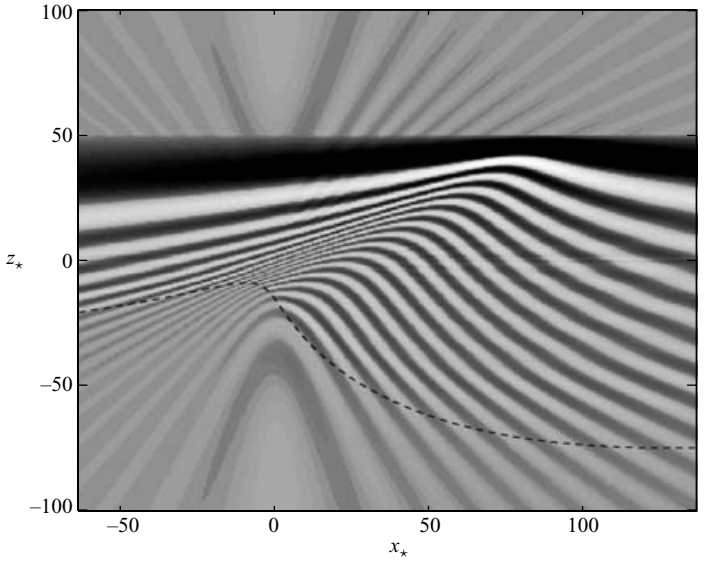


FIGURE 7. The internal potential field for both transient start-up waves and permanent waves. The point source was towed with $\alpha = \pi/3$. The field shown is at $t_\star = 100$ and $y_\star = 10$.

method for achieving this is given in Bleistein (1966, § 5), Bleistein & Handelsman (1986, § 9.4) and Felsen & Marcuvitz (1994, § 4.6), and an outline of the method is presented here. Let

$$I(\lambda) = \int_0^\infty f(\tau) \exp\left\{ \mathrm{i}\left[\lambda g(\tau) - \frac{\pi}{4} \right] \right\} \mathrm{d}\tau, \tag{2.34}$$

https://doi.org/10.1017/S0022112006001571 Published online by Cambridge University Press

where f and g are analytic functions in some domain, $\mathscr{D}$, containing the contour of integration, $\tau = 0$ and $\tau = \tau_s$ where g has a simple saddle, i.e.

$$g'(\tau_s) = 0, \qquad g''(\tau_s) \neq 0. \tag{2.35}$$

The phase g is replaced by

$$g(\tau) - g(0) = \mu \left[\frac{q^2}{2} + aq \right], \tag{2.36}$$

where

$$\mu = \mathrm{sgn}(g''(\tau_s)), \quad a = -\mathrm{sgn}(\tau_s)\sqrt{2|g(\tau_s) - g(0)|}. \tag{2.37}$$

Then substitution of (2.37) into (2.34) gives

$$I(\lambda) = \exp\left\{ \mathrm{i}\left[\lambda g(0) - \frac{\pi}{4} \right] \right\} \int_0^\infty \left(f(\tau) \frac{\mathrm{d}\tau}{\mathrm{d}q} \right) \exp\left\{ \mathrm{i}\lambda\mu \left[\frac{q^2}{2} + aq \right] \right\} \mathrm{d}q. \tag{2.38}$$

The contour of integration is rotated using $q = \zeta \mathrm{e}^{\mathrm{i}\mu\pi/4}$. It follows that, provided f and g are suitably well behaved as $\tau \to \infty$, then

$$I(\lambda) = \exp\left\{ \mathrm{i}\left[\lambda g(0) - \frac{\pi}{2} H(-\mu) \right] \right\} \int_0^\infty G(\zeta) \mathrm{e}^{-\lambda(\zeta^2/2 + b\zeta)} \, \mathrm{d}\zeta, \tag{2.39}$$

where $b = a\mathrm{e}^{-\mathrm{i}\mu\pi/4}$ and $G(\zeta) = f(\tau)\mathrm{d}\tau/\mathrm{d}q$. Without loss of generality, the function G is then written as

$$G(\zeta) = \sigma_0 + \zeta\sigma_1 + \zeta(\zeta + b)G_1(\zeta), \tag{2.40}$$

for some function G_1. Evaluating G at $\zeta = 0$ and $\zeta = -b$ gives

$$\sigma_0 = \frac{f(0)\mu a}{g'(0)}, \quad \sigma_0 - b\sigma_1 = \frac{f(\tau_s)}{\sqrt{|g''(\tau_s)|}}, \tag{2.41}$$

respectively. Defining

$$V_r(s) = \int_0^\infty \zeta^r \mathrm{e}^{-[\zeta^2/2 + s\zeta]} \mathrm{d}\zeta, \tag{2.42}$$

it follows from (2.39), (2.40) and (2.42) that

$$I(\lambda) \sim \exp\left\{ \mathrm{i}\left[\lambda g(0) - \frac{\pi}{2} H(-\mu) \right] \right\} \left\{ \frac{\sigma_0}{\lambda^{1/2}} V_0(\sqrt{\lambda} b) + \frac{\sigma_1}{\lambda} V_1(\sqrt{\lambda} b) \right\} + O\left(\frac{1}{\lambda^{3/2}} \right). \tag{2.43}$$

The functions V_0 and V_1 may be straightforwardly expressed in terms of Fresnel integrals, and it follows that

$$\begin{aligned} I(\lambda) \sim & \sqrt{\frac{\pi}{2\lambda|g''(\tau_s)|}} f(\tau_s) \exp\left\{ \mathrm{i}\left[\lambda g(\tau_s) - \frac{\pi}{2} H(-\mu) \right] \right\} \\ & \times \left\{ 1 + (1 - \mathrm{i}\mu)(\mathscr{C} + \mathrm{i}\mu\mathscr{S}) \left[\sqrt{\frac{2\lambda}{\pi}|g(\tau_s) - g(0)|} \right] \mathrm{sgn}(\tau_s) \right\} \\ & + \mathrm{i}\frac{\mu\,\mathrm{sgn}(\tau_s)}{\lambda} \exp\left\{ \mathrm{i}\left[\lambda g(0) - \frac{\pi}{4} \right] \right\} \left[\frac{f(\tau_s)}{\sqrt{2|g''(\tau_s)|\,|g(\tau_s) - g(0)|}} - \frac{f(0)}{|g'(0)|} \right], \end{aligned} \tag{2.44}$$

with errors of $O(\lambda^{-3/2})$. It can be shown that if additional assumptions are made regarding the separation of τ_s from 0, such that (2.31) holds, then using the result

https://doi.org/10.1017/S0022112006001571 Published online by Cambridge University Press

that for $x \in \mathbb{R}_{\geqslant 0}$

$$(\mathscr{C} \pm \mathscr{S})(x) \sim \frac{1 \pm \mathrm{i}}{2} \mp \frac{\mathrm{i}}{\pi x} \exp\left\{ \pm \mathrm{i} \frac{\pi x^2}{2} \right\} \text{ as } x \to \infty, \tag{2.45}$$

applied to (2.44) recovers the non-uniform approximation (2.26*a*).

2.4. *Application of the composite uniform and general uniform expansions*

In contrast with the non-uniform approximation of Voisin (1994), both the composite uniform approximation (2.32) and the general uniform approximation (2.44) are uniformly valid as $\tau_s \to 0$ (i.e. as the causality envelope is approached in space), for a given time. Hence, both approximations remove both the unphysically large velocities and the phase shift predicted by the existing non-uniform approximation to the wave field (2.26) close to the causality envelope. There are some differences between the application of the two approximations however.

When the composite uniform approximation (2.32) is applied, exactly the same method of application may be employed as with the non-uniform approximations (Voisin 1994). The permanent wave contributions can be calculated individually and the causality condition that $0 \leqslant \tau_s \leqslant t$ can be applied. The superposition of the permanent waves and the transient wave contributions may then be found.

With the general uniform approximation (2.44), the condition that $0 \leqslant \tau_s$ is automatically applied, due to the range of integration over which $V_r(s)$ is defined, (2.42). The condition that $\tau_s \leqslant t$ can still be applied by discarding any contribution to the permanent wave field (the $O(\lambda^{-1/2})$ term in (2.44)) if $\tau_s > t$. However, an added complication exists with the general uniform approximation compared to the composite uniform approximation. The $O(\lambda^{-1})$ transient wave contribution in the general uniform approximation (2.44) explicitly depends on the retarded time τ_s. For regions of interference, where more than one permanent wave contributes to the wave field (Scase & Dalziel 2004), this necessarily introduces a problem as the transient wave field must be included only once in the superposition. One possible remedy is to use the general uniform approximation for the permanent wave with smallest τ_s and then add on permanent waves using the standard non-uniform approximation (the $O(\lambda^{-1/2})$ term in (2.26*a*)). This is less satisfactory than the simple use of the composite uniform approximation. For the remainder of the present paper we will simply employ the composite uniform approximation for this reason.

2.5. *Extended sources and viscous attenuation*

In order to make a meaningful comparison between the theoretical results described above and laboratory experiments, the finite size of the source generating the waves and the effect of the viscosity found in real fluids are taken into account. As in Dupont & Voisin (1996), Scase (2003) and Scase & Dalziel (2004), the internal wave field for an extended source, in this case a sphere, can be approximated from the point-source solution. The calculated internal potential should simply be multiplied by the spatial Fourier transform of the source.

The same source as in Dupont & Voisin (1996), Scase (2003) and Scase & Dalxiel (2004) is used here, namely

$$m(\boldsymbol{r}, t) = \frac{3}{2a} \{ \boldsymbol{v}_0 \cdot \boldsymbol{r}(t) \} \delta(|\boldsymbol{r}(t)| - a), \tag{2.46}$$

https://doi.org/10.1017/S0022112006001571 Published online by Cambridge University Press

and the Fourier transform of this source is given by

$$M(\boldsymbol{k}, t) = \int_{\mathbb{R}^3} m(\boldsymbol{r}, t)\, \mathrm{e}^{\mathrm{i}\boldsymbol{k}\cdot\boldsymbol{r}}\, \mathrm{d}\boldsymbol{r} = 6\mathrm{i}\pi a^3 (\boldsymbol{v}_0 \cdot \boldsymbol{k}) \frac{j_1(ka)}{ka}, \tag{2.47}$$

where j_1 is a spherical Bessel function of the first kind. For the transient gravity waves

$$\omega = \frac{N|z|}{r}, \quad \boldsymbol{c}_g = \frac{\boldsymbol{r}}{t}, \quad \boldsymbol{k} = \frac{\omega}{c_g}\left(\frac{\boldsymbol{r}}{r} - \frac{r}{z}\hat{\boldsymbol{e}}_z\right), \tag{2.48}$$

where $c_g = |\boldsymbol{c}_g|$.

That viscosity acts to attenuate internal waves is well known and has been considered by many authors (e.g. Lighthill 1978; Dupont 1995). Viscous attenuation on internal waves generated by a horizontally towed cylinder was considered by Stevenson, Chang & Laws (1979) and viscous attenuation on internal waves generated by either a horizontally or vertically towed cylinder was considered by Stevenson, Woodhead & Kanellopulos (1983). Derivations for the effective strength of the viscous attenuation based on a given internal wave's wavenumber are provided in both Lighthill (1978) and Dupont (1995). Viscous attenuation of the energy of the waves is at a rate $\nu|\boldsymbol{k}|^2$ per unit time, which is equivalent to $\nu|\boldsymbol{k}|^4/(Nk_z)$ per unit distance along the wave beams. As derived by Dupont (1995), to take into account the effects of viscosity, the internal potential for a given gravity wave obtained without viscosity must be multiplied by

$$\exp\left\{-\frac{\nu|\boldsymbol{k}|^3 R^2}{2N R_h}\right\}. \tag{2.49}$$

It follows simply from (2.49) that the waves which are most severely damped by viscosity are the short-wavelength, large-wavenumber waves.

3. Experimental technique

A variety of experimental techniques are available for visualizing internal waves. Classical methods include interferometry (see Van Dyke 1982, e.g. figures 83 and 143), shadowgraph visualizations (a technique often associated with the visualization of shock fronts; see Van Dyke 1982), schlieren visualizations, and visualization by the use of Moiré fringes. Interferometry involves splitting phase-locked light into two beams. One beam passes through the experimental tank and the other passes around the tank via a set of mirrors for example. The beams are brought back together on a visualising surface. This technique gives quantifiable data for the fluid density at given heights within the tank, but is extremely sensitive and so experimentally intricate. Examples of internal wave visualisation by classical schlieren include Mowbray & Rarity (1967*a*, *b*) and Stevenson (1968). An example of internal wave visualisation by Moiré fringes is included in Sakai (1990). These methods rely on the same underlying physical process. As the density of a medium is increased, the speed of light propagation through this medium is decreased. A perturbation to the density field corresponds to a perturbation to the refractive index field. Perturbations to the density field therefore cause deflections in the light rays which can then interfere both constructively and destructively. It is these regions of interference which are visualized. All three methods have significant disadvantages when quantitative information about the density field is required and an extensive discussion of some of these deficiencies is provided in Dalziel *et al.* (2000). Visualizing regions of constructive and destructive interference does not provide enough information about how the light rays have been

https://doi.org/10.1017/S0022112006001571 Published online by Cambridge University Press

deflected for the inverse problem, of finding the perturbation to the density field, to be solved. The deficiencies of these experimental techniques have largely been overcome by a method known as 'synthetic schlieren'.

Previously synthetic schlieren has only been used in two dimensions, usually in a Cartesian frame (Sutherland *et al.* 1999, 2000) and more recently in an axisymmetric set-up (Flynn *et al.* 2003). However, these arrangements are not suitable for analysing the internal waves generated by a sphere translating at arbitrary angle to the vertical, where the flow is fully three-dimensional. Hence, a different approach is used here.

It is important to note that this modification to the experimental technique will only produce a breadth-averaged measurement of the gradients of density perturbation or vertical velocity. This method cannot produce fully three-dimensional information about the flow. However, these measurements can be compared directly to breadth-averaged quantities predicted by the theory of § 2.

3.1. *Overview of two-dimensional synthetic schlieren*

The path of a light ray passing through a medium with refractive index field $n(x, z)$ is governed by the following coupled ordinary differential equations (Weyl 1954):

$$\frac{\mathrm{d}^2\xi}{\mathrm{d}y^2} = \left[1 + \left(\frac{\mathrm{d}\xi}{\mathrm{d}y}\right)^2 + \left(\frac{\mathrm{d}\zeta}{\mathrm{d}y}\right)^2\right]\frac{1}{n}\frac{\partial n}{\partial x}, \tag{3.1a}$$

$$\frac{\mathrm{d}^2\zeta}{\mathrm{d}y^2} = \left[1 + \left(\frac{\mathrm{d}\xi}{\mathrm{d}y}\right)^2 + \left(\frac{\mathrm{d}\zeta}{\mathrm{d}y}\right)^2\right]\frac{1}{n}\frac{\partial n}{\partial z}, \tag{3.1b}$$

where the position of the light ray is given by $\boldsymbol{x} = (\xi(y), y, \zeta(y))$. Equations (3.1*a*) and (3.1*b*) can be derived from the eikonal equation in the form

$$\left(\frac{\mathrm{d}}{\mathrm{d}s}\left[n\frac{\mathrm{d}x}{\mathrm{d}s}\right], \frac{\mathrm{d}}{\mathrm{d}s}\left[n\frac{\mathrm{d}z}{\mathrm{d}s}\right]\right) = \left(\frac{\partial n}{\partial x}, \frac{\partial n}{\partial z}\right), \tag{3.2}$$

where $\mathrm{d}s = \sqrt{1+\xi'^2+\zeta'^2}\,\mathrm{d}y$, $\mathrm{d}n/\mathrm{d}y = \xi'\partial n/\partial x + \zeta'\partial n/\partial z$ and a prime denotes differentiation with respect to y.

By assuming that deflections to the path of the light ray are small† (i.e. that $\mathrm{d}\xi/\mathrm{d}y \ll 1$ and $\mathrm{d}\zeta/\mathrm{d}y \ll 1$) equations (3.1) are decoupled as

$$\frac{\mathrm{d}^2\xi}{\mathrm{d}y^2} = \frac{1}{n}\frac{\partial n}{\partial x}, \qquad \frac{\mathrm{d}^2\zeta}{\mathrm{d}y^2} = \frac{1}{n}\frac{\partial n}{\partial z}, \tag{3.3}$$

which gives

$$\xi(y) = \xi_i + y\tan\phi_\xi + \frac{y^2}{2n}\frac{\partial n}{\partial x}, \quad \zeta(y) = \zeta_i + y\tan\phi_\zeta + \frac{y^2}{2n}\frac{\partial n}{\partial z}, \tag{3.4a, b}$$

for $y \in [0, W]$, where ϕ_ζ is as in figure 8. If the refractive index is decomposed as $n(\boldsymbol{x}) = n_{00} + n_0(z) + n'(\boldsymbol{x})$, where n_{00} is a nominal reference refractive index, $n_0(z)$ represents spatial variations associated with the known base state (i.e. the background stratification) and $n'(\boldsymbol{x})$ is the perturbation to this initial state generated by the flow, then the shift in the apparent origin of the light ray is given by

$$(\Delta\xi_a, \Delta\zeta_a) = \frac{W(W+2B)}{2}\frac{1}{n_{00}}\left(\frac{\partial n'}{\partial x}, \frac{\partial n'}{\partial z}\right), \tag{3.5}$$

† This assumption can be avoided, as pointed out by Dr L. Maas, Royal Netherlands Institute for Sea Research, see the Appendix.

https://doi.org/10.1017/S0022112006001571 Published online by Cambridge University Press

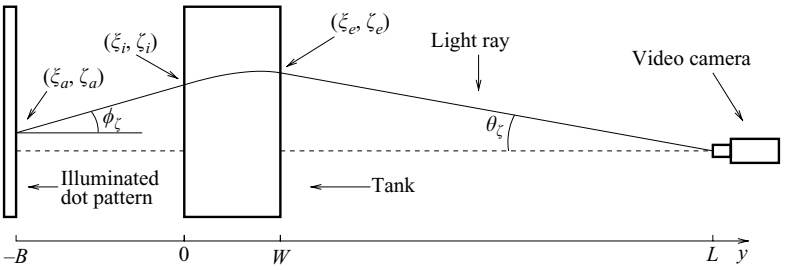


FIGURE 8. Experimental set-up for synthetic schlieren. The apparent origin of the light ray is at (ξ_a, ζ_a); it is incident on the back of the tank at (ξ_i, ζ_i) and exits the tank at (ξ_e, ζ_e).

where B is the distance from the illuminated dot pattern to the back of the experimental tank and W is the width of the tank (see figure 8). To a good approximation, the relationship between the density of the fluid and the refractive index is linear with

$$\nabla n = \frac{\mathrm{d}n}{\mathrm{d}\rho}\nabla\rho = \beta\frac{n_{00}}{\rho_{00}}\nabla\rho, \tag{3.6}$$

where $\beta \approx 0.184$ (Weast 1981). Hence the relationship between the density perturbation to the flow field and the apparent shift in the origin of a given light ray is

$$(\Delta\xi_a, \Delta\zeta_a) = \frac{W(W+2B)}{2}\frac{\beta}{\rho_{00}}\left(\frac{\partial\rho'}{\partial x}, \frac{\partial\rho'}{\partial z}\right). \tag{3.7}$$

3.2. *Modification for three-dimensional experiments*

3.2.1. *Optics*

By considering the tank to be split into m thin, vertical, equally sized slices with normals parallel to the y-axis and neglecting the variation of refractive index with y across each slice, so that the refractive index is given by

$$n(\boldsymbol{x}) = \begin{cases} n_{\mathrm{air}}, & -B \leqslant y < 0 \\ n^{(r)}(x, z), & \dfrac{r-1}{m}W \leqslant y < \dfrac{r}{m}W \\ n_{\mathrm{air}}, & W \leqslant y \leqslant L \end{cases} \tag{3.8}$$

for $r = 1, \ldots, m$, the system of equations (3.1) is solved. This is achieved by solving the decoupled ordinary differential equations (3.3) in the rth slice and then matching the tangents of the light ray path at the edge of each slice, starting at the camera and tracing back towards the light source. From (3.4*a*), in the rth slice the path $\zeta^{(r)}(y)$ must satisfy

$$\zeta^{(r)}(y) = a_0 + a_1 y + \frac{y^2}{2n}\frac{\partial n}{\partial z}, \tag{3.9}$$

for two constants a_0 and a_1. These constants allow the tangents at the front and back of each slice to be matched to the surrounding slices, meaning that the light ray is continuous and differentiable. This process generates the difference equation

$$\frac{\zeta^{(r-1)} - 2\zeta^{(r)} + \zeta^{(r+1)}}{\Delta^2} = c^{(r)} + c^{(r+1)}, \tag{3.10}$$

https://doi.org/10.1017/S0022112006001571 Published online by Cambridge University Press

where

$$c^{(r)} = \frac{1}{2n^{(r)}}\frac{\partial n^{(r)}}{\partial z}, \quad \text{and} \quad \Delta = \frac{W}{m}. \tag{3.11}$$

The constants $\zeta_i = \zeta^{(0)}$ and $\zeta_e = \zeta^{(m)}$. Matching tangents on the back of the tank yields the result

$$\Delta\zeta_a = \frac{W}{2m}\sum_{r=1}^{m}\left\{\left[\frac{W}{m}(2r-1)+2B\right]\frac{\beta}{\rho_{00}}\frac{\partial\rho'^{(r)}}{\partial z}\right\}. \tag{3.12a}$$

A similar calculation can be performed for $\Delta\xi_a$ giving

$$\Delta\xi_a = \frac{W}{2m}\sum_{r=1}^{m}\left\{\left[\frac{W}{m}(2r-1)+2B\right]\frac{\beta}{\rho_{00}}\frac{\partial\rho'^{(r)}}{\partial x}\right\}. \tag{3.12b}$$

Note that the two-dimensional formulæ (3.7) are recovered by setting all the $\rho'^{(r)}$ terms equal.

Equation (3.12) is simply a weighted average according to how close the rth slice is to the front of the tank, $y = W$. This is expected since a small deflection of the light ray at the front of the tank causes a larger shift in the apparent origin of the light ray than a deflection of the same size at the back of the tank. In the limit $m \to \infty$ (3.12) becomes

$$(\Delta\xi_a, \Delta\zeta_a) = \frac{\beta}{\rho_{00}}\int_0^W (y+B)\left(\frac{\partial\rho_1}{\partial x}, \frac{\partial\rho_1}{\partial z}\right)\mathrm{d}y. \tag{3.13}$$

If the flow is symmetrical about the plane $y = W/2$ then the results (3.12) and (3.13) can be simplified to give, for m even

$$(\Delta\xi_a, \Delta\zeta_a) = \frac{W(W+2B)}{m}\sum_{r=1}^{m/2}\frac{\beta}{\rho_{00}}\left(\frac{\partial\rho'^{(r)}}{\partial x}, \frac{\partial\rho'^{(r)}}{\partial z}\right), \tag{3.14a}$$

for m odd

$$(\Delta\xi_a, \Delta\zeta_a) = \frac{W(W+2B)}{m}\left\{\left[\sum_{r=1}^{(m-1)/2}\frac{\beta}{\rho_{00}}\left(\frac{\partial\rho'^{(r)}}{\partial x}, \frac{\partial\rho'^{(r)}}{\partial z}\right)\right] + \frac{\beta}{2\rho_{00}}\left(\frac{\partial\rho'^{([m+1]/2)}}{\partial x}, \frac{\partial\rho'^{([m+1]/2)}}{\partial z}\right)\right\}, \tag{3.14b}$$

and in the limit $m \to \infty$

$$(\Delta\xi_a, \Delta\zeta_a) = \frac{\beta(W+2B)}{\rho_{00}}\int_0^{W/2}\left(\frac{\partial\rho'}{\partial x}, \frac{\partial\rho'}{\partial z}\right)\mathrm{d}y, \tag{3.14c}$$

which can be derived directly from (3.3) by integration by parts. Equations (3.14) are not weighted averages because deflections are occurring in pairs, centred on the middle of the tank, $y = W/2$. This averaging process will be referred to as 'breadth averaging'.

3.2.2. *Application to sphere towing experiments*

The most simple application to a 'sphere towing' experiment is to compare the gradients of the measured, breadth-averaged density perturbation (3.12)–(3.13) to the theory of § 2. It follows from (2.3) that

$$\nabla\rho'_p \sim -\frac{m_0\rho_0 N^3}{2\pi g}\frac{R_h}{R^4 c_g^2|A|^{1/2}}\cos\left[\frac{N|R_z|}{c_g}+\frac{\pi}{2}H(A)\right]\left(R_xR_z, R_yR_z, -R_h^2\right). \tag{3.15}$$

https://doi.org/10.1017/S0022112006001571 Published online by Cambridge University Press

Ensuring that the sphere is towed in the central plane of the tank means that the simplified results (3.14) can be used.

It is possible to directly infer the vertical velocity field in the special case of a sphere towed steadily for a long time, such that transient waves may be considered negligible. Then, the surrounding wave field is in a steady state, such that $\partial/\partial t \equiv -\boldsymbol{v}_0 \cdot \nabla$. From the linearized Euler equations, it follows that

$$\frac{\partial \rho'}{\partial t} + w\frac{\mathrm{d}\rho_0}{\mathrm{d}z} = 0,$$

and therefore

$$w \approx \frac{g}{N^2 \rho_{00}} \boldsymbol{v}_0 \cdot \nabla \rho'. \tag{3.16}$$

This relationship allows the comparison of the perturbed density field with the vertical velocity field as well as comparison with the gradients of the density fields.

3.3. *Experimental set-up*

The experimental tank had dimensions 2.5 m × 0.7 m × 0.8 m Behind the tank was a 2.0 m × 1.0 m light bank using 6 pairs of 70 W high-frequency (28 kHz) fluorescent tubes. A digital Atmel-Grenoble Camelia 8 Megapixel camera was used to capture the experiments. The camera's resolution was 3500 × 2300 pixels and the images were digitized to 12 bits. This camera was used in conjunction with an LCD shutter and a Nikon zoom lens (Nikkor 35 ~ 135 mm F 3.5 ~ 4.5). The area of the experiment visualized was approximately 1.0 m × 0.6 m, with $B = 1.15$ m, $L = 3.10$ m.

The stratification was created using the well-known 'double-buckets' technique (Fortuin 1960). This technique creates nominally linear density stratifications, but these were found to be extremely close to the exponential distributions assumed in the analysis of § 2, differing by at most 0.02 % for the range of densities considered here.

The dot pattern on the mask consisted of transparent dots placed a random perturbation away from a regular grid. The dots were of size 1 mm on a black background, with a relative diameter of dot to mean spacing of 0.25. A Perspex sphere of diameter 4×10^{-2} m was towed through the fluid by a stainless steel rod of diameter 4×10^{-3} m driven by a motor. The rod was held at a constant angle by a guide attached to the motor.

As a preliminary check on the experimental technique, an initial unperturbed image of the dot pattern was captured with the sphere out of the tank. The sphere was then very slowly pushed through the tank to the full extent of the rod. The fluid was then allowed to settle. After a long time the images of the dots returned to their unperturbed positions. The initial unperturbed image is referred to as the 'reference image'.

After the fluid has come to rest, the sphere is then towed through the tank and the perturbations to the dot pattern are recorded and compared with the pattern in the reference image. The data are then processed to give the gradient of the density perturbation fields.

4. Results

Figure 9 is a comparison between the analysis presented in § 2 and experiment. In the experiment $\mathscr{F} = 0.23$, $\mathscr{R} = 180$ and $\alpha = 60.0°$. The calculated vertical gradient of density perturbation fields in figure 9(*a–e*) have a resolution of 300 × 300 and

https://doi.org/10.1017/S0022112006001571 Published online by Cambridge University Press

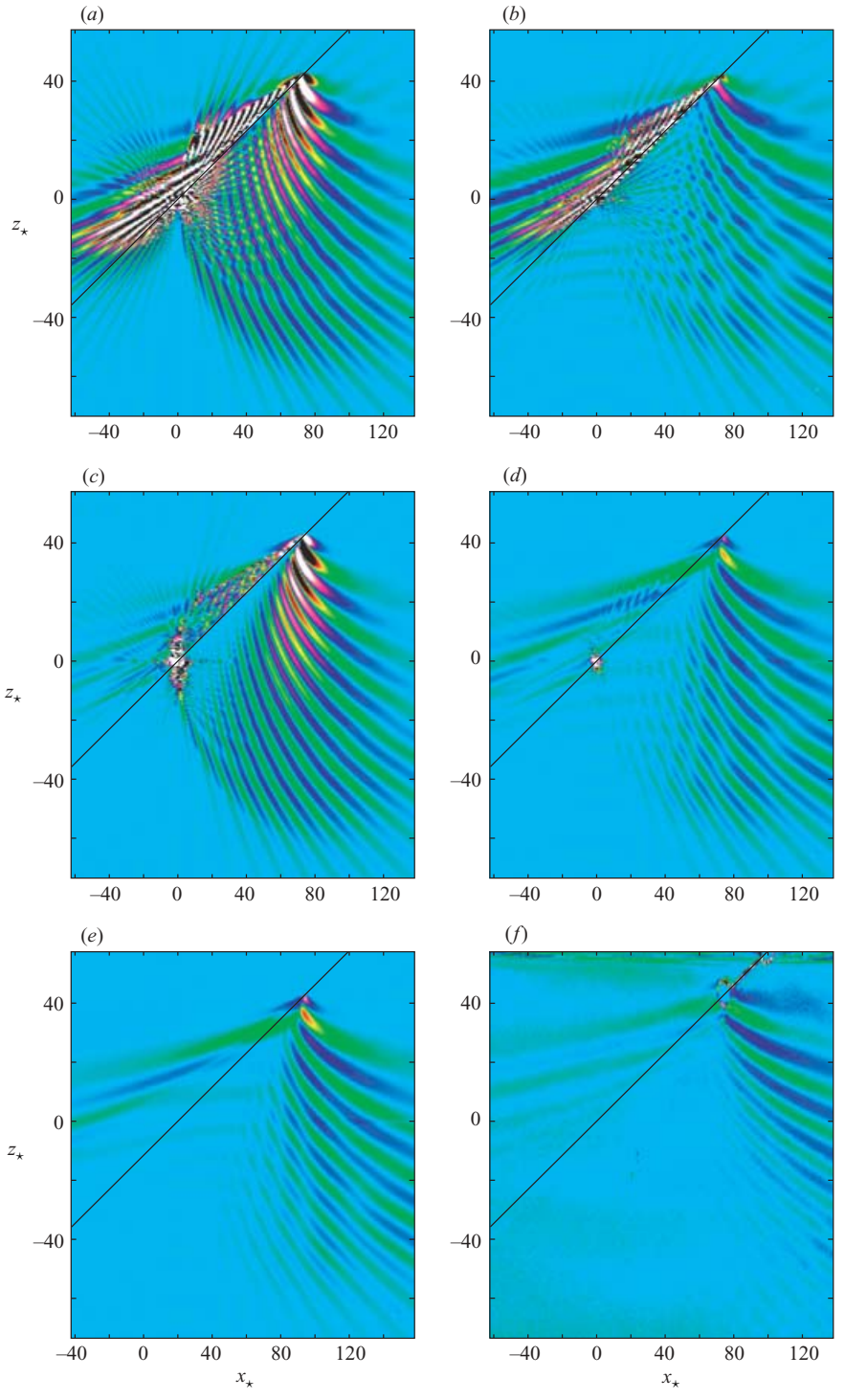


FIGURE 9. For caption see facing page.

https://doi.org/10.1017/S0022112006001571 Published online by Cambridge University Press

where they have been breadth averaged it has been done over 300 slices, as described in § 3.2. The analytical model used in all the figures in this section was the composite uniform model of § 2.2. Figure 9(*a*) is the point-source model in the centreplane $y_\star = 0$.† Figure 9(*b*) is the point-source model but breadth averaged in the $y_\star$-direction. The effect of this averaging is a homogenization of the wave amplitudes with respect to the distance from the source. As can be seen, the apparent amplitude of the waves near the source in 9(*b*) is much smaller than in 9(*a*). Figures 9(*c*)–9(*d*) are the same as figures 9(*a*)–9(*b*) except with a spherical source instead of a point source generating the flow field. Again the breadth averaging homogenizes the wave amplitudes with respect to distance from the source. The differences in the internal waves generated between the point source and the spherical source is most clearly seen in the centreplane, $y_\star = 0$ (i.e. figures 9*a* and 9*c*). The interference patterns caused by the finite size of the source are most clearly observed beneath the tow line. There is strong destructive interference exhibited by the spherical source leading to much smaller-amplitude waves below the tow line than for the point source. Figure 9(*e*) is the same as figure 9(*d*) but includes attenuation of the waves due to viscosity. As was seen in § 2.5 the viscosity damps the higher-frequency waves and so the interference region in the cone above the tow line (Scase & Dalziel 2004) is less apparent.

The theory compares well with the experimental result, figure 9(*f*). The most obvious discrepancy is that the phase near to the source is shifted. The error near to the source is expected since the analysis in § 2 is asymptotic and is only valid far away from the source.

Although the sphere was towed slowly to minimize the size of the trailing wake some wake was unavoidable with the present experimental set-up. (Note that the 'wake' referred to here is the classical wake left behind a towed body, e.g. Batchelor (1967, § 5.12) and not the wave pattern behind a towed body, e.g. Kelvin's ship wake (e.g. Thomson 1891; Lighthill 1978).) The effect of this wake was to destroy the coherency of the fluid motions immediately behind the sphere and thus disrupt the generation of the internal waves. Hence, in the region between the tow line and vertically below the sphere in the experimental figure 9(*f*), fewer waves are visible than in the theoretical figure 9(*e*).

As the sphere is impulsively started, a fan of waves is produced. These waves can propagate ahead of the sphere and reflect off the free surface of the fluid in the tank. These reflections are of small amplitude and have been ignored.

Figure 11 is a comparison of the analysis in § 2.2 with experiment. Unlike figure 9, in figure 11(*a*, *b*), $\alpha = 30°$, $\mathscr{F} = 0.28$ and $\mathscr{R} = 200$ and in figure 11(*c*, *d*), $\alpha = 2.9°$, $\mathscr{F} = 0.48$ and $\mathscr{R} = 350$. Figure 11(*a*) is the calculated vertical gradient of the density perturbation field, using the spherical-source model with viscous attenuation, for the

† The structure is the same as would be observed for a line (cylinder) source, apart from a difference in amplitude (Scase 2003).

FIGURE 9. Comparison of analysis from § 2.2 with experiment. The sphere, radius $a = 2.1 \times 10^{-2}$ m has been towed at $\alpha = \pi/3$ for $t = 86.0$ s. The buoyancy frequency $N = 0.91\,\mathrm{s}^{-1}$, the reference density of the stratification is $\rho_{00} = 1041\,\mathrm{kg\,m}^{-3}$, the tow speed is $v_0 = 4.5 \times 10^{-3}$ m s^{-1} and the kinematic viscosity is $\nu = 1.0 \times 10^{-6}\,\mathrm{m^2\,s^{-1}}$. The field shown is the vertical gradient of the density perturbation field: (*a*) the point-source model in the $y = 0$ plane; (*b*) the breadth-averaged model; (*c*) the sphere model in the $y = 0$ plane; (*d*) the breadth-averaged sphere model; (*e*) the breadth-averaged sphere model with viscous attenuation of waves; (*f*) the experimental result. The colour bar is shown in figure 10.

https://doi.org/10.1017/S0022112006001571 Published online by Cambridge University Press

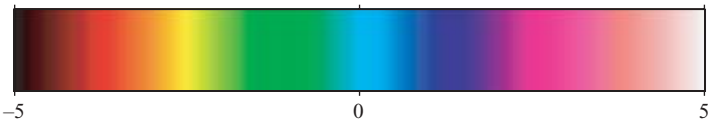


FIGURE 10. Colour bar for figures 9 and 11. The units are kg m^{-4}.

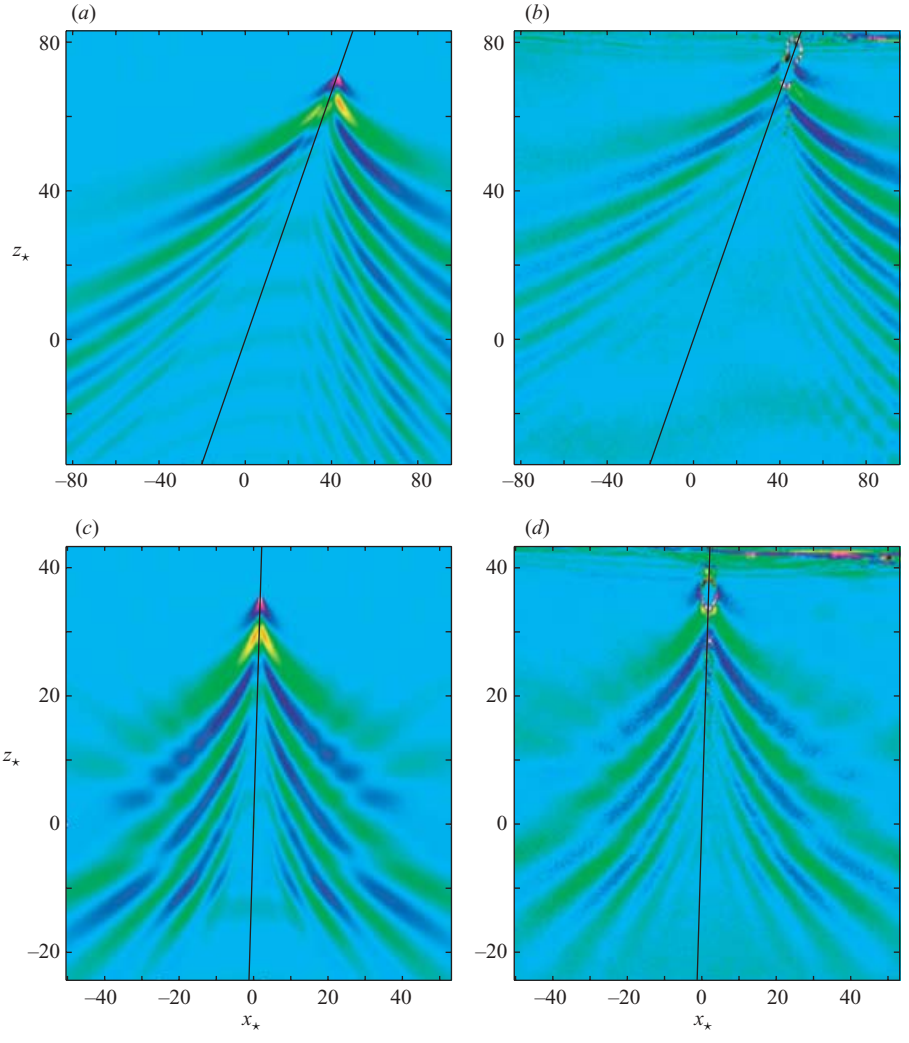


FIGURE 11. Comparison of analysis from § 2.2 (a, c) with experiment (b, d). The angle of tow is $\alpha = 31.0^\circ$ and the tow speed is $v_0 = 5.1 \times 10^{-3}$ m s^{-1} in (a) and (b), whereas $\alpha = 2.9^\circ$ and the tow speed is $v_0 = 8.8 \times 10^{-3}$ m s^{-1} in (c) and (d). The other flow parameters are as in figure 9. The field shown is the vertical gradient of the density perturbation field. (a) and (c) are calculated using the spherical source model with viscous attenuation of the waves. The colour bar in figure 10 shows the scale.

experiment shown in figure 11(b). Good general agreement is shown between the theory and the experiment. The wake behind the sphere can also clearly be seen in figure 11. There is good agreement both far from and near to the source in

https://doi.org/10.1017/S0022112006001571 Published online by Cambridge University Press

figure 11(c, d) which is equivalent to figure 11(a, b) but for a tow angle of $\alpha = 2.9°$. However, as discussed below and illustrated in figure 12 there is some misalignment of the surfaces of constant phase.

Smirnov & Chashechkin (1998) used a dipolar source model of the form

$$m(\boldsymbol{r}, t) = m_0[\Delta(\boldsymbol{r} - \boldsymbol{v}_0 t + \boldsymbol{a}) - \Delta(\boldsymbol{r} - \boldsymbol{v}_0 t - \boldsymbol{a})], \tag{4.1}$$

where $\boldsymbol{a} = \hat{\boldsymbol{v}}_0 a$ 'is the vector of distance between the source and the sink'. They found that their calculated wavefronts did not align with their experimental results and suggest

> 'The best agreement between theoretical and experimental phase surfaces corresponds to the position of a virtual source on the line of motion at a distance of 1.4 cm upstream from the centre of the [1 cm diameter] sphere.'

They further suggest that some of this misalignment is due to 'some variations in the buoyancy frequency'. It is possible that this is part of the reason for the discrepancies between the theoretical calculations and the experimental figures in the present study since the errors in measuring the Froude number and the non-dimensionalization scale are not large enough to account for the discrepancies alone.

The error in measuring the frame rate of the camera is estimated to be 0.5 % and the error in measuring the positional shift of the sphere between the initial and final images is also estimated to be 0.5 %. This gives an approximate error in calculating the speed of the sphere as 1 %. Errors due to parallax are largely avoided by defining a real-world coordinate system (for use in calculating distances from the experimental images) when a grid with known mesh size is submerged in the stratified fluid. The greatest single source of errors in the sphere towing experiments comes from the calculation of the buoyancy frequency. Typically the calculated error estimates in curve fitting to the data were 1 %. The sphere that was towed through the tank had a diameter of 4×10^{-2} m $\pm$ 0.05 %. This leads to an approximate error in the calculation in both the Froude number and the non-dimensionalization of the axes of 2 %.

Figure 12 compares the theoretical values for the vertical gradient of the density perturbation field along the line $x_\star = -10$ from figure 11(c) to the experimental values found in figure 11(d). The dotted curve was measured from experiment. The solid curve is the calculated theoretical amplitude. The theoretical line has been moved vertically up a non-dimensional distance 2. This corresponds to a dimensional distance of 1.9×10^{-2} m, just under one sphere radius. As was noted, Smirnov & Chashechkin (1998) also found the better agreement between experiment and theory by offsetting the source.

The agreement between the theory and the experiment in figure 12 is good. There is some experimental noise around $z_\star = 0$ caused by the camera looking at the surface of the water in the tank. Internal reflection of the light means that the camera can see a dot pattern in the surface of the water. There is inevitably some surface disturbance as the sphere is towed through the tank; this disturbance causes very large perturbations to the dot image reflected by the surface and thus synthetic schlieren falsely registers extreme density changes. Figure 12 shows that the theory predicts the phase speed and the amplitude of the waves very well.

The evidence from figures 9, 11 and 12 suggests that there is generally good agreement between the linear theoretical model and the experiments, as was also found by Stevenson (1968), Stevenson & Thomas (1969), Peat & Stevenson (1975) and Smirnov & Chashechkin (1998). Good agreement was found between the linear theoretical

https://doi.org/10.1017/S0022112006001571 Published online by Cambridge University Press

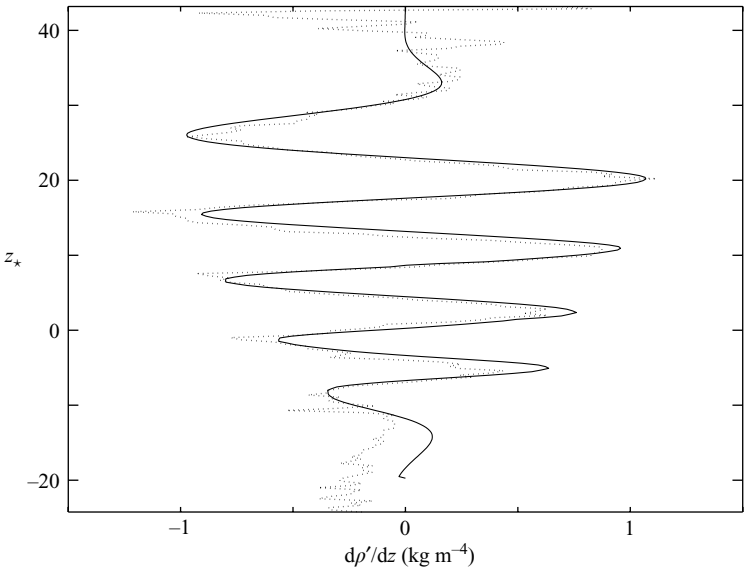


FIGURE 12. Comparison of the amplitudes of the vertical gradient of the density perturbation field for the theory in figure 11(*c*) (solid line) with the experiment in figure 11(*d*) (dashed line) along the line $x_\star = -10$. The amplitude has been averaged over the breadth of the tank (i.e. over $y_\star$ as described in § 3.2).

model and the experiments within the causality envelope in Scase (2003, chap. 6); however transient waves were not included theoretically, and so no waves were predicted outside the causality envelope.

5. Conclusions

In an attempt to compare experiments with the theoretical models of Voisin (1994) and Scase & Dalziel (2004) it was discovered that Voisin's description of transient start-up waves was inappropriate. The predicted waves had unphysically large velocities near the boundary of the causality envelope. The origin of this difficulty was that the model used a non-uniform approximation to the internal potential. In § 2.2 the unphysical velocities were removed using a composite uniform approximation to the wave field. The modified expression for the transient start-up waves predicted physically realistic velocities for the waves. A further benefit of this composite uniform approximation is that it means that the internal potential field, and hence the velocity field and pressure fields, are continuous and differentiable across the boundary of the causality envelope.

The theory underlying synthetic schlieren has been developed for use with three-dimensional flows. Although the new theory is not fully three-dimensional, it allows comparison of breadth-averaged experiments and theory. This technique was applied to internal wave fields generated by a sphere towed through a density-stratified fluid. The use of synthetic schlieren has allowed the visualization of large areas of internal wave generation. Comparison with theory has required the careful calculation of both the permanent wave field built up by the motion of the source and also the transient wave field created when the source is impulsively started.

The evidence from figures 9, 11 and 12 suggests that there is generally good agreement between the theoretical model and the experiments, as was also found by

https://doi.org/10.1017/S0022112006001571 Published online by Cambridge University Press

Stevenson (1968), Stevenson & Thomas (1969), Peat & Stevenson (1975) and Smirnov & Chashechkin (1998). It was found (as seen previously by Smirnov & Chashechkin 1998) that a small offset of the theoretical source was required in order to get the best phase agreement (figure 12). The new analysis provides a more physically realistic treatment of transient start-up waves. The synthetic schlieren experimental technique allows much larger areas of the wave field to be visualized than has previously been possible.

The authors would like to acknowledge the comments of an anonymous referee which lead to a much clearer description of the results presented in §§ 2.2–2.4. This work was partially funded by studentship NER/S/A/2000/03262 from the Natural Environment Research Council who also provided support for the development of the experimental techniques under grant NER/B/S/2001/00242.

Appendix. Light ray equations without linearization

Equations (4*a*) and (4*b*) in Dalziel *et al.* (2000) (equations (3.1) in the present paper) can be solved without making the approximation of small $\mathrm{d}\xi/\mathrm{d}y$, $\mathrm{d}\zeta/\mathrm{d}y$. Let $\chi(y) = \mathrm{d}\xi/\mathrm{d}y$ and $\kappa(y) = \mathrm{d}\zeta/\mathrm{d}y$. Then dividing (3.1*a*) by (3.1*b*) gives

$$\frac{\mathrm{d}\chi}{\mathrm{d}\kappa} = \frac{\partial n/\partial x}{\partial n/\partial z} = \sigma, \tag{A 1}$$

where σ is defined as the ratio of the gradients of the refractive indices and is independent of y. Since $\chi(0) = \tan\phi_\xi = \xi_0'$ and $\kappa(0) = \tan\phi_\zeta = \zeta_0'$, it follows that

$$\chi(y) = \sigma(\kappa(y) - \zeta_0') + \xi_0'. \tag{A 2}$$

Thus, using equation (3.1*b*),

$$\frac{\mathrm{d}\kappa}{\mathrm{d}y} = \{1 + [\sigma(\kappa - \zeta_0') + \xi_0']^2 + \kappa^2\}\frac{1}{n}\frac{\partial n}{\partial z}. \tag{A 3}$$

Defining $\gamma^2 = 1 + \sigma^2 + (\xi_0' - \sigma\zeta_0')^2$ it follows that

$$\begin{aligned}\xi = \xi_0 - \frac{1}{2(1+\sigma^2)\partial n/\partial x}\Bigg\{ & 2y\frac{\partial n}{\partial x}(\sigma\zeta_0' - \xi_0') \\ & + 2\sigma^2 n \log\left|\cos\left\{\frac{y|\sigma\gamma|}{\sigma^2 n}\frac{\partial n}{\partial x} + \tan^{-1}\left[\frac{\sigma(\zeta_0' + \sigma\xi_0')}{|\sigma\gamma|}\right]\right\}\right| \\ & + \sigma^2 n \log\left[\frac{(1+\zeta_0'^2+\xi_0'^2)(1+\sigma^2)}{\gamma^2}\right]\Bigg\},\end{aligned} \tag{A 4}$$

and similarly

$$\begin{aligned}\zeta = \zeta_0 + \frac{1}{2(1+\sigma^2)\partial n/\partial z}\Bigg\{ & 2y\frac{\partial n}{\partial x}(\sigma\zeta_0' - \xi_0') \\ & - 2n \log\left|\cos\left\{\frac{y|\gamma|}{n}\frac{\partial n}{\partial z} + \tan^{-1}\left[\frac{\zeta_0' + \sigma\xi_0'}{|\gamma|}\right]\right\}\right| \\ & - n \log\left[\frac{(1+\zeta_0'^2+\xi_0'^2)(1+\sigma^2)}{\gamma^2}\right]\Bigg\}.\end{aligned} \tag{A 5}$$

https://doi.org/10.1017/S0022112006001571 Published online by Cambridge University Press

By calculating the ratio of the right-hand side to the left-hand side of equations (4*a*) and (4*b*) in Dalziel *et al.* and expanding as a series in y, the fractional error in the linearization approximation is given as

$$\frac{1}{1+\zeta_0'^2+\xi_0'^2}-\frac{2}{n\left(1+\zeta_0'^2+\xi_0'^2\right)^2}\left(\xi_0'\frac{\partial n}{\partial x}+\zeta_0'\frac{\partial n}{\partial z}\right)y+O(y^2), \tag{A 6}$$

which shows that the small-deviation approximation leads to a small but systematic error.

REFERENCES

Batchelor, G. K. 1967 *An Introduction to Fluid Dynamics*. Cambridge University Press, Cambridge Mathematical Library Edition 2000.

Bleistein, N. 1966 Uniform asymptotic expansions of integrals with stationary point near algebraic singularity. *Commun. Pure Appl. Maths* **19**, 353–370.

Bleistein, N. & Handelsman, B. A. 1986 *Asymptotic Expansions of Integrals*. Dover.

Boussinesq, J. 1903 *Théorie Analytique de la Chaleur*, Volume 2. Paris: Gathier-Villars.

Bretherton, F. P. 1967 The time-dependent motion due to a cylinder moving in an unbounded rotating or stratified fluid. *J. Fluid Mech.* **28**, 545–570.

Chashechkin, Yu. D. & Makarov, S. A. 1984 Time-varying internal waves. *Dokl. Earth Sci. Sect.* **276**, 210–213. (Translation from *Dokl. Akad. Nauk SSSR*, **276**, 1246–1250.)

Dalziel, S. B., Hughes, G. O. & Sutherland, B. R. 2000 Whole-field density measurements by 'synthetic schlieren'. *Exps. Fluids* **28**, 322–335.

Dupont, P. 1995 Ondes internes engendrées par une source oscillante en mouvement. PhD. thesis., L'Université Joseph Fourier, Grenoble.

Dupont, P. & Voisin, B. 1996 Internal waves generated by a translating and oscillating sphere. *Dyn. Atmos. Oceans* **23**, 289–298.

Felsen, L. B. & Marcuvitz, N. 1994 *Radiation and Scattering of Waves*. Prentice-Hall.

Flynn, M. R., Onu, K. & Sutherland, B. R. 2003 Internal wave excitation by a vertically oscillating sphere. *J. Fluid Mech.* **494**, 65–93.

Fortuin, J. M. H. 1960 Theory and application of two supplementary methods of constructing density gradient columns. *J. Polymer Sci.* **44**, 505–515.

Gorodtsov, V. A. & Teodorovich, E. V. 1980 On the generation of internal waves in the presence of uniform straight-line motion of local and nonlocal sources. *Izv. Atmos. Ocean. Phys* **16**, 9 699–704. (Translation from *Izv. Akad. Nauk SSSR Fiz. Atmos. Okeana* **16**, 954–961.)

Hart, R. W. 1981 Generalised scalar potentials for linearized three-dimensional flows with vorticity. *Phys. Fluids* **24**, 1418–1420.

Hinch, E. J. 1991 *Perturbation Methods*. Cambridge University Press.

Lighthill, M. J. 1978 *Waves in Fluids*. Cambridge University Press.

Mowbray, D. E. & Rarity, B. S. H. 1967*a* A theoretical and experimental investigation of the phase configuration of internal waves of small amplitude in a density stratified liquid. *J. Fluid Mech.* **28**, 1–16.

Mowbray, D. E. & Rarity, B. S. H. 1967*b* The internal wave pattern produced by a sphere moving vertically in a density stratified liquid. *J. Fluid Mech.* **30**, 489–495.

Peat, K. S. & Stevenson, T. N. 1975 Internal waves around a body moving in a compressible density-stratified fluid. *J. Fluid Mech.* **70**, 673–688.

Rarity, B. S. H. 1967 The two-dimensional wave pattern produced by a disturbance moving in an arbitrary direction in a density stratified liquid. *J. Fluid Mech.* **30**, 329–336.

Reitz, J. R. & Milford, F. J. 1960 *Foundations of Electromagnetic Theory*. Addison-Wesley.

Sakai, S. 1990 Visualisation of internal gravity waves by Moiré method. *Kashika-Joho* **10**, 65–68.

Scase, M. M. 2003 Vortex rings in a stratified fluid. PhD thesis, University of Cambridge.

Scase, M. M. & Dalziel, S. B. 2004 Internal wave fields and drag generated by a translating body in a stratified fluid. *J. Fluid Mech.* **498**, 289–313.

https://doi.org/10.1017/S0022112006001571 Published online by Cambridge University Press

Smirnov, S. A. & Chashechkin, Yu. D. 1998 Internal lee (joined) waves at an arbitrary orientation of the incident flow. *Izv. Atmos. Ocean Phys.* **34**, 475–482. (Translation from *Izv. Akad. Nauk Fiz. Atmos. Okeana* **34**, 528–536.)

Stevenson, T. N. 1968 Some two-dimensional internal waves in a stratified fluid. *J. Fluid Mech.* **33**, 715–720.

Stevenson, T. N. 1973 The phase configuration of internal waves around a body moving in a density stratified fluid. *J. Fluid Mech.* **60**, 759–767.

Stevenson, T. N., Chang, W. L. & Laws, P. 1979 Viscous effects in lee waves. *Geophys. Astrophys. Fluid Dyn.* **13**, 141–151.

Stevenson, T. N. & Thomas, N. H. 1969 Two-dimensional internal waves generated by a travelling oscillating cylinder. *J. Fluid Mech.* **36**, 505–511.

Stevenson, T. N., Woodhead, T. J. & Kanellopulos, D. 1983 Viscous effects in some internal waves. *Appl. Sci. Res.* **40**, 185–197.

Sturova, I. V. 1980 Internal waves generated in an exponentially stratified fluid by an arbitrarily moving source. *Fluid Dyn.* **15**, 378–383. (Translation from *Izv. Akad. Nauk SSSR Mekh. Zhid. i Gaza* (3), 67–74.)

Sutherland, B. R., Dalziel, S. B., Hughes, G. O. & Linden, P. F. 1999 Visualisation and measurement of internal waves by 'synthetic schlieren'. Part 1. Vertically oscillating cylinder. *J. Fluid Mech.* **390**, 93–126.

Sutherland, B. R., Dalziel, S. B., Hughes, G. O. & Linden, P. F. 2000 Internal waves revisited *Dyn. Atmos. Oceans* **31**, 209–232.

Thomson, W. 1891 *Popular Lectures.* Vol. 3, pp. 450–500. Macmillan.

Van Dyke, M. 1982 *An Album of Fluid Motion.* Parabolic Press, Stanford.

Voisin, B. 1991 Internal wave generation in uniformly stratified fluids. Part 1. Green's function and point sources. *J. Fluid Mech.* **231**, 439–480.

Voisin, B. 1994 Internal wave generation in uniformly stratified fluids. Part 2. Moving point sources. *J. Fluid Mech.* **261**, 333–374.

Weast, R. C. 1981 *Handbook of Chemistry and Physics.* CRC. Press.

Weyl, F. J. 1954 Analysis of optical methods. In *Physical Measurements in Gas Dynamics and Combustion* (ed. R. W. Ladenburg), pp. 3–25. Princeton University Press.

Woodhead, T. J. 1983 The phase configuration of the waves around an accelerating disturbance in a rotating stratified fluid. *Wave Motion* **5**, 157–165.

https://doi.org/10.1017/S0022112006001571 Published online by Cambridge University Press